JOURNAL OF COMPUTATIONAL PHYSICS **134,** 203–215 (1997)
ARTICLE NO. CP975681

Smoothed Particle Hydrodynamics for the Simulation of Broken-Ice Fields: Mohr–Coulomb-Type Rheology and Frictional Boundary Conditions

Ricardo Gutfraind[1,2] and Stuart B. Savage

Department of Civil Engineering & Applied Mechanics, McGill University, Montreal, Quebec, Canada H3A 2K6

Received June 19, 1996; revised February 17, 1997

A rheology based on the Mohr–Coulomb yield criterion is implemented in the framework of smoothed particle hydrodynamics (SPH). We apply this approach to the simulation of broken-ice fields floating on the water surface and moving under the effect of wind forces. When broken-ice fields are regarded as a continuum, their rheological behavior can be described by a model known as viscous-plastic. In this approach the ice field is modeled as a viscous fluid for very small strain rates and is assumed to flow plastically otherwise. It is in the plastic regime that the stress states are described in terms of the Mohr–Coulomb yield criterion. Besides broken-ice fields, numerous other problems in the field of quasi-static granular flows can be characterized by this type of rheological behavior. We first show how the momentum equations for a Mohr–Coulomb-type rheology are implemented in the framework of SPH. For most granular flow systems, the moving interior particles are bounded by fixed frictional walls and one must also model these boundary conditions. A Coulomb-friction condition is applied within the framework of SPH. This type of boundary is implemented by means of a wall that exerts a normal potential force of repulsion on the SPH particles, combined with a tangential force proportional to the normal force. The approach can be applied to model flows adjacent to straight walls as well to more complicated boundaries.

1. INTRODUCTION

Smoothed Particle Hydrodynamics (SPH) was invented by Lucy [1, 2] to study problems in astrophysics. These problems are usually characterized by masses that move in unbounded three-dimensional spaces. The fluids involved in these applications have very low viscosities and are generally approximated as inviscid. The first applications of SPH to problems involving other components of the stress tensor, besides the pressure, have appeared recently in the literature. Libersky and Petschek [3] have formulated an elastic, perfectly plastic constitutive model within the framework of SPH. Since then, SPH has been successfully applied to the study of the deformation of a metal cylinder resulting from the normal impact against a flat, rigid surface [4, 5], to the modelling of fractures in brittle solids [6], and to the simulation of viscous flows [7]. In this work, we look at the implementation of SPH to treat a viscous-plastic rheology, used for the simulation of broken-ice fields driven by the wind and water currents.

Ice fields on rivers and oceans are often made up of discrete blocks (usually called floes), whose sizes in the horizontal direction can range from a few meters in the summer to several kilometers in the winter. The movement of the floes is driven by the wind and water currents. The floes dissipate energy through collisions and rubbing frictional contacts with other floes, as well as through frictional drag due to the water on their bottom surface. Many works have dealt with the modeling of the rheological behavior of the ice field when it is regarded as a continuum. These include, models based on plasticity theory [8], elastic-plastic models [9], and the viscous-plastic model proposed by Hibler [10, 11]. Hilber's viscous-plastic approach is probably the most widely used in the field. In this approach, the ice is modeled as a viscous fluid for small strain rates, whereas for large strain rates the ice is assumed to flow in a plastic manner. It is in the plastic regime that the stress states are described in terms of the Mohr–Coulomb yield criterion.

The zone of ice near its edge, away from the Artic basin is usually called the marginal ice zone (MIZ). Ice forecasting in the MIZ is of crucial importance for problems such as navigation and off-shore oil operations. The precise prediction of the ice-edge location is important information in all these operations. Until recently, all the numerical methods used for solving ice-forecasting problems used finite differences implemented on Eulerian fixed grids. In order to avoid problems of artificial diffusion present in the Eulerian fixed grids, Pritchard *et al.* [12] proposed the use of an adaptive grid. In an attempt to move further towards a Lagrangian approach, Flato [13] proposed the use of the particle-in-cell (PIC) method. Due to its fully

[1] Corresponding author.
[2] Present address: Hyprotech, 300 Hyprotech Centre, 1110 Centre Street N, Calgary, AB, Canada T2E 2R2.

0021-9991/97 $25.00

Lagrangian characteristics, SPH can be a very useful tool for the study of this type of problem.

In many ice forecasting problems, the presence of a nearby coast plays an important role in the generation of ice stresses as well as in the determination of ice drift velocities. As was mentioned above, SPH has been usually implemented for problems involving unbounded spaces. Implementations of solid boundaries in SPH have only recently appeared in the literature. In order to model nonfrictional boundaries for the simulation of incompressible inviscid flows, Monaghan [14] used fixed particles that exert central forces which repel the SPH particles. Takeda *et al.* [7] used ghost particles to model nonslip boundary conditions for the simulation of viscous flows. In the present work, we model frictional solid surfaces by using a wall which exerts a normal force of repulsion on the SPH particles, combined with a tangential force whose magnitude is proportional to the normal force (Coulomb friction law). We apply this type of boundary condition to model a straight coast and a corner-shaped coast in the problem of broken-ice fields. We note that this approach can be easily extended to other problems which require the modelling of friction surfaces characterized by the Coulomb friction law (i.e., quasi-static granular flows and other problems in soil mechanics).

The present paper is organized as follows. In Section 2, we review the models used to described broken-ice fields driven by wind drag and water currents. In Section 3, we briefly review the features of SPH and show how to implement the momentum equations in SPH for a Mohr–Coulomb rheology. In Section 4, the features of the numerical implementation of SPH are discussed. We look at the approaches for modeling solid boundaries and we discuss some features concerning the time-stepping. In Section 5, we briefy discuss the application of discrete-particle simulations for the modeling of broken-ice fields. These are molecular-dynamic type methods, in which each ice block is treated individually as it moves under the influence of the wind and water drag and it interacts through collisions and friction with the other ice blocks. No rheological modeling is involved in this discrete approach, other than those involved in contact force dynamics. Results from the discrete-particle simulations are compared with the results obtained by using SPH (for a detailed discussion of the implementation of this method for the simulation of broken-ice fields; see Refs. [15–17]). In Section 6, the detailed numerical results are presented. Two cases are analyzed: the ice moving next to a straight coast and the ice moving next to a corner-shaped coast.

2. BROKEN-ICE FIELDS: MODELS AND GOVERNING EQUATIONS

Typically, the ice field is made up of individual blocks or floes whose horizontal dimensions are much larger than their thickness and the ice pack can be considered as a two-dimensional system. The floes, as they move, interact with the other floes through collisions and friction forces. If the ice pack is modeled as a continuum, then one looks at the stresses generated due to the ice floe interactions, and the stress–strain relation has to be described in terms of a rheological law.

The equations of motion for the ice pack regarded as a continuum are given by

$$\rho h_{\text{ice}} \frac{d\mathbf{v}}{dt} = -h_{\text{ice}} \nabla \cdot \boldsymbol{\sigma} - \rho h_{\text{ice}} f \mathbf{k} \times \mathbf{v} + (\boldsymbol{\tau}_a - \boldsymbol{\tau}_w), \quad (1)$$

where $\mathbf{k}$ is a unit vector in the vertical direction pointing towards the sky, f is the Coriolis parameter, ρ is the ice-pack density, $\boldsymbol{\sigma}$ is the stress that arises from the interactions between the ice floes, $\boldsymbol{\tau}_a$ and $\boldsymbol{\tau}_w$ are the air and water stresses (drag forces per unit of ice surface), and h_{ice} is the thickness of the ice pack (in the vertical direction). The Coriolis parameter f is defined as $f = \Omega \sin \theta$, where Ω is the velocity of rotation of the earth and θ is the latitude. The air and water stresses are given by

$$\boldsymbol{\tau}_a = C_a(\cos \alpha + \sin \alpha \mathbf{k}\times)\mathbf{V}_a, \quad (2)$$

$$\boldsymbol{\tau}_w = -C_w(\cos \beta + \sin \beta \mathbf{k}\times)\mathbf{v}, \quad (3)$$

where $\mathbf{V}_a$ is the geostrophic wind velocity, C_a and C_w are the air and water drag coefficients, and α and β are the air and water turning angles, respectively (see below). In Eq. (2) it has been assumed that the ice velocity is negligible in comparison with the wind velocity; and in Eq. (3) it has been assumed that the water velocity, outside the water boundary layer next to the ice surface, is negligible in comparison to the ice velocity $\mathbf{v}$, namely the effect of the water currents is not considered.

The presence of the angles α and β in Eqs. (2) and (3) can be explained as follows. The geostrophic wind is the wind outside the earth boundary layer, where friction effects between the air and the earth surface (in our case the ice field) can be neglected. Here, the air moves due to the pressure gradient, which at steady state is only balanced by the Coriolis force. Next to the earth surface, due to the friction between the air and the earth surface, the wind velocity is reduced and its limiting direction at the surface is turned an angle α, counter clockwise with respect to the geostrophic-wind direction. This explains the presence of the angle α in Eq. (2). The presence of the angle β in Eq. (3), associated with the difference between the direction of the water shear stress and the (negative) ice velocity vector, can be explained in a similar manner. These concepts are explained in detail in the field literature (for instance, see Ref. [18]). In this work, we will concentrate on the implementation in the framework of SPH, of a

rheology of Mohr–Coulomb-type and of frictional solid boundaries. There will be no comparisons with field data.

Substituting Eqs. (2) and (3) in Eq. (1) and decomposing it in its x and y components, one obtains

$$\rho h_{\text{ice}} \frac{du}{dt} = -h_{\text{ice}} \left(\frac{\partial \sigma_x}{\partial x} + \frac{\partial \tau}{\partial y} \right) + \rho h_{\text{ice}} f v + C_a (U_a \cos \alpha - V_a \sin \alpha) + C_w (v \sin \beta - u \cos \beta), \quad (4)$$

$$\rho h_{\text{ice}} \frac{dv}{dt} = -h_{\text{ice}} \left(\frac{\partial \sigma_y}{\partial y} + \frac{\partial \tau}{\partial x} \right) - \rho h_{\text{ice}} f u + C_a (U_a \sin \alpha + V_a \cos \alpha) - C_w (v \cos \beta + u \sin \beta), \quad (5)$$

where u and v as well as U and V denote x and y components of the ice and wind velocities, respectively. The physical values for the ice properties, wind and water drag coefficients and Coriolis parameter selected for the present study are

$\rho = 0.91 \times 10^3$ kg m^{-3}
$f = 1.44 \times 10^{-4}$ s^{-1}
$C_w = 0.652$ kg m^{-2} s^{-1}
$C_a = 0.0126$ kg m^{-2} s^{-1}
$h_{\text{ice}} = 1$ m
$\alpha = \beta = 22.5°$.

In order to solve Eqs. (4) and (5) one needs some type of rheological law. The approach that has been most widely used in the last few years to describe the rheological behavior of sea ice is Hibler's viscous-plastic model [11]. In the viscous-plastic approach, the ice shear strength is introduced by using a nonlinear viscosity which is selected so that the ice flows as a viscous fluid for small strain rates and in a plastic manner otherwise. Stress states in the plastic regime are evaluated based on the Mohr–Coulomb yield criterion

$$\sigma_1 - \sigma_2 = (\sigma_1 + \sigma_2) \sin \phi, \quad (6)$$

where σ_1 and σ_2 are the principal stresses and ϕ is the internal friction angle (Fig. 1a). The stress due to ice-floe interactions expressed in terms of the nonlinear viscosity is

$$\sigma_{ij} = P \delta_{ij} - 2\eta (\dot{\varepsilon}_{ij} - \tfrac{1}{2} \dot{\varepsilon}_{kk} \delta_{ij}), \quad (7)$$

where P is the pressure (taken as positive for compressive stresses), η is the viscosity, and $\dot{\varepsilon}_{ij}$ is the strain-rate tensor.

Assuming that the principal axes of stress and strain rate coincide and using the Mohr–Coulomb yield criterion to characterize the plastic regime, the stress state of the ice

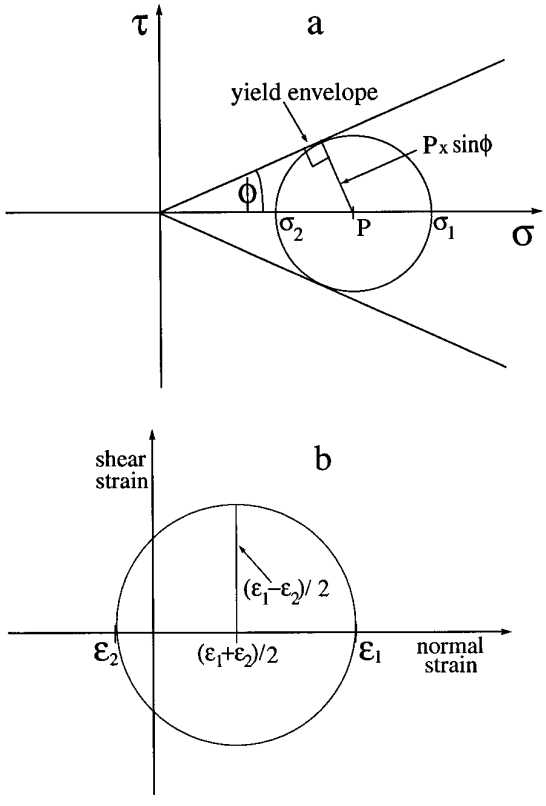

FIG. 1. Mohr circle: (a) for the stresses and (b) for the strain rates. The principal components of the stress are σ_1 and σ_2; and the principal components of the strain rate are ε_1 and ε_2.

can be described by using the following expression for the viscosity

$$\eta = \min \left\{ \frac{P \sin \phi}{\dot{\varepsilon}_1 - \dot{\varepsilon}_2}, \eta_{\max} \right\}, \quad (8)$$

where $\dot{\varepsilon}_1$ and $\dot{\varepsilon}_2$ are the principal components of the strain-rate tensor (Fig. 1b), and $\eta_{\max}$, the maximum value of the viscosity, determines whether the stress state is inside or on the yield envelope. When $\eta = \eta_{\max}$, the ice will flow as a viscous fluid, whereas it will flow in a plastic manner (stress independent of strain rate) when η is smaller than $\eta_{\max}$. The value of $\eta_{\max}$ is usually set in such a way that the stress state will be on the yield envelope in most of the simulation domain. Hence, one should use a very large value of $\eta_{\max}$, so that this value is reached only in zones of very small strain rates. However, a very large value of $\eta_{\max}$ can lead to numerical instabilities, and therefore, one has to compromise between the two possibilities. The value used in most of the simulations in this work is $\eta_{\max} = 1 \times 10^{11}$ *Kg* m^{-1} s^{-1}. Knowing the strain-rate tensor and the pressure, and assuming coincidence of principal axes of stress and strain rate, enables one to determine the

whole stress tensor. Notice that for stress states on the yield envelope ($\eta < \eta_{\max}$), Eqs. (7) and (8) also imply stress independent of strain rate as expected in the plastic regime.

In order to estimate the pressure, a pressure-density relation in the form of an equation of state is necessary. For broken-ice fields at high areal concentrations, the concentration variations during drift are not large. Thus, any equation that is able to model the broken-ice field as almost incompressible is appropriate for the purpose of this work. The following form has been chosen for the equation of state

$$P = \gamma \frac{\rho - \rho_0}{\rho_{\max} - \rho}, \tag{9}$$

where ρ_0 is the initial density of the broken-ice field (taken as the density of the solid ice times the fraction of the surface occupied by the ice). The parameters of the equation of state such as γ and $\rho_{\max}$ have to be chosen in such a way that they produce relatively small density variations in the range of pressures for the problem under consideration. The ice is expected to present no resistance to tensile forces, so no negative pressures are allowed, and when $\rho < \rho_0$, the pressure is set to zero.

3. SPH: BASIC FEATURES AND MOMENTUM EQUATIONS

In this section we briefly review the basic concepts of SPH (for a detailed review, see for instance Refs. [19–21]), and we show how to obtain the SPH form of the momentum equations for a rheology of Mohr–Coulomb-type. A field variable can be expressed by using the integral

$$f(\mathbf{r}) = \int f(\mathbf{r}')\delta(\mathbf{r} - \mathbf{r}')\, d\mathbf{r}', \tag{10}$$

and it can then be approximated by using an interpolation kernel

$$\langle f(\mathbf{r})\rangle = \int f(\mathbf{r}')W(\mathbf{r} - \mathbf{r}', h)\, d\mathbf{r}', \tag{11}$$

where $W(\mathbf{u}, h)$ is a kernel having the properties

$$\int W(\mathbf{u}, h)\, d\mathbf{u} = 1 \tag{12}$$

and

$$\lim_{h\to 0} W(\mathbf{u}, h) = \delta(\mathbf{u}). \tag{13}$$

The kernel most commonly used (and the one used in the present work) is the Gaussian, which in two dimensions is given by

$$W(\mathbf{u}, h) = \frac{1}{\pi h^2} \exp(-u^2/h^2). \tag{14}$$

For a fluid of density $\rho(\mathbf{r})$, the right-hand side of Eq. (11) is expressed as

$$\int [f(\mathbf{r}')/\rho(\mathbf{r}')]W(\mathbf{r} - \mathbf{r}', h)\rho(\mathbf{r}')\, d\mathbf{r}', \tag{15}$$

and the integral (15) is evaluated, dividing the space into volume elements having a mass m_k,

$$\langle f(\mathbf{r})\rangle \simeq \sum_{k=1}^{N} m_k \frac{f_k}{\rho_k} W(\mathbf{r} - \mathbf{r}_k, h), \tag{16}$$

where $f_k \equiv f(\mathbf{r}_k)$.

The kernel estimate of ∇f is

$$\langle \nabla f(\mathbf{r})\rangle \simeq \int W(\mathbf{r} - \mathbf{r}')\nabla f(\mathbf{r}')\, d\mathbf{r}'. \tag{17}$$

Integrating by parts and assuming that W approaches zero fast enough so that the surface terms vanish, one obtains

$$\begin{aligned} \langle \nabla f(\mathbf{r})\rangle &\simeq \int \nabla W(\mathbf{r} - \mathbf{r}', h) f(\mathbf{r}')\, d\mathbf{r}' \\ &\simeq \sum_{k=1}^{N} \frac{m_k}{\rho_k} f_k \nabla_i W_{ik}, \end{aligned} \tag{18}$$

where $\nabla W(\mathbf{r} - \mathbf{r}', h)$ is the gradient with respect to $\mathbf{r}$, ∇_i is the gradient with respect to the coordinates of particle i and $W_{ik} \equiv W(\mathbf{r}_i - \mathbf{r}_k, h)$.

The density is usually evaluated by using the continuity equation, which in its SPH form is given by

$$\frac{d\rho_i}{dt} = -\rho_i \int \mathbf{v}\nabla W\, d\mathbf{r}' \simeq \rho_i \sum_k \frac{m_k}{\rho_k} (\mathbf{v}_i - \mathbf{v}_k)\nabla_i W_{ik}. \tag{19}$$

In obtaining the right-hand side of Eq. (19), the following term has been subtracted from the integral in Eq. (19),

$$\rho_i \mathbf{v}_i \int \nabla W\, d\mathbf{r}' \simeq \rho_i \mathbf{v}_i \sum_k \frac{m_k}{\rho_k} \nabla_i W_{ik}, \tag{20}$$

which is zero because the kernel vanishes at infinity. If one uses Eq. (16) to evaluate the density, the kernel estimate of the density can drop near the edges of the fluid. With Eq. (19) the density varies only when there is relative movement between particles. This is the approach we used

in the present work to avoid the drop in density near the ice edge.

In order to evaluate the forces acting on individual particles, a symmetric form of the momentum equation is generally used in which the pressure gradient is substituted by [19],

$$\frac{1}{\rho}\nabla P = \nabla\left(\frac{P}{\rho}\right) + \frac{P}{\rho^2}\nabla\rho. \tag{21}$$

This form is preferred because it leads to an exact conservation of momentum. In order to find the kernel estimate of Eqs. (4) and (5), the divergence of the stress is transformed by using the same identity used for the pressure gradient in Eq. (21). The equations are then multiplied by the kernel, integrated, and the integrals are approximated as discrete sums

$$\begin{aligned}\frac{du_i}{dt} = &-\sum_k m_k\left[\frac{\sigma_{x,k}}{\rho_k^2}+\frac{\sigma_{x,i}}{\rho_i^2}\right]\frac{\partial W_{ik}}{\partial x_i}\\ &-\sum_k m_k\left[\frac{\tau_k}{\rho_k^2}+\frac{\tau_i}{\rho_i^2}\right]\frac{\partial W_{ik}}{\partial y_i}+fv_i\\ &+\frac{1}{\rho_i h_{\text{ice}}}C_a(U_a\cos\alpha - V_a\sin\alpha)\\ &+\frac{1}{\rho_i h_{\text{ice}}}C_w(v_i\sin\beta - u_i\cos\beta),\end{aligned} \tag{22}$$

$$\begin{aligned}\frac{dv_i}{dt} = &-\sum_k m_k\left[\frac{\sigma_{y,k}}{\rho_k^2}+\frac{\sigma_{y,i}}{\rho_i^2}\right]\frac{\partial W_{ik}}{\partial y_k}\\ &-\sum_k m_k\left[\frac{\tau_k}{\rho_k^2}+\frac{\tau_i}{\rho_i^2}\right]\frac{\partial W_{ik}}{\partial x_i}-fu_i\\ &+\frac{1}{\rho_i h_{\text{ice}}}C_a(U_a\sin\alpha + V_a\cos\alpha)\\ &-\frac{1}{\rho_i h_{\text{ice}}}C_w(v_i\cos\beta - u_i\sin\beta).\end{aligned} \tag{23}$$

The kernel estimate of the strain rate tensor is

$$\dot{\varepsilon}_{xx} = \sum_k \frac{m_k}{\rho_k}(u_k-u_i)\frac{\partial W_{ik}}{\partial x_i},\quad \dot{\varepsilon}_{yy} = \sum_k \frac{m_k}{\rho_k}(v_k-v_i)\frac{\partial W_{ik}}{\partial y_i},$$
$$\dot{\varepsilon}_{xy} = \frac{1}{2}\left(\sum_k \frac{m_k}{\rho_k}(v_k-v_i)\frac{\partial W_{ik}}{\partial x_i}+\sum_k \frac{m_k}{\rho_k}(u_k-u_i)\frac{\partial W_{ik}}{\partial y_i}\right), \tag{24}$$

where x_i and y_i in $\partial W_{ik}/\partial x_i$ and $\partial W_{ik}/\partial y_i$, respectively, denote differentiation with respect to the coordinates of particle i. By substituting (24) in (7) and (8), the stress tensor components are evaluated and these are then substituted in (22) and (23) to evaluate the forces acting on the individual particles.

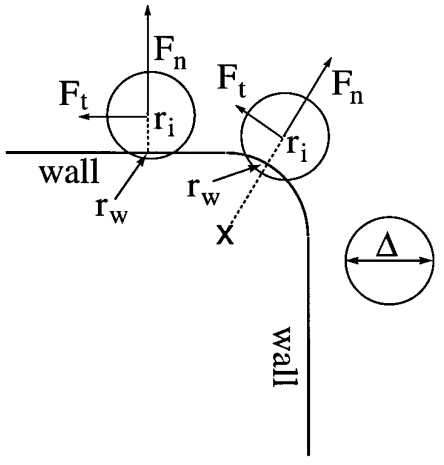

FIG. 2. Implementation of a solid boundary by using a wall that exerts a normal force of repulsion on the SPH particles, in combination with a tangential friction force. The wall position vector r_w is located at the intersection of the wall and the normal to the wall from the particle centre (dashed lines). The **x** indicates the centre of curvature of the curved part of the wall, whose radius of curvature $R_{\text{curv}} = \Delta$. The vectors $\mathbf{F}_n$ and $\mathbf{F}_t$ are the normal force and the tangential frictional force, respectively.

4. NUMERICAL IMPLEMENTATION OF SPH: SOLID BOUNDARIES AND TIME STEPPING

4.1. *Solid Boundaries*

A solid boundary is simulated by using a wall that exerts a normal force of repulsion on the SPH particles, combined with a tangential friction force proportional to the normal force (Coulomb's law). In order to model the effects of the wall, one assigns to the SPH particles an imaginary diameter (in this case equal to the initial distance between particle centers, Δ). The magnitude of the normal force acting on the particle is proportional to the overlap between the particle and the wall (Fig. 2)

$$\mathbf{F}_n = \beta_{bc}(\Delta/2 - |\mathbf{r}_i - \mathbf{r}_w|)\mathbf{n} \tag{25}$$

when $\Delta/2 > |\mathbf{r}_i - \mathbf{r}_w|$; otherwise $\mathbf{F}_n = 0$. In Eq. (25), $\mathbf{r}_i$ and $\mathbf{r}_w$ are the position vectors of the particle i and the wall, respectively; $\mathbf{n}$ is a unit vector normal to the wall direction at the contact between the particle and the wall; $\mathbf{F}_n$ is the resulting normal force; and β_{bc} is a proportionality constant that has to be adjusted in order to avoid large overlap between the wall and the particles. The tangential friction force is proportional to the normal force

$$\mathbf{F}_t = -\mu|\mathbf{F}_n|\mathbf{t}, \tag{26}$$

where **t** is a unit vector tangential to the wall and pointing in the direction of the particle velocity, and μ is the wall friction coefficient, here taken to be equal to $\sin\phi$ (cf. (8)).

Notice that the corner in Fig. 2 has been smoothed by using a quarter of circle of radius Δ, which joins the two perpendicular parts of the wall. We found that this manner of implementing the corner in the solid wall prevents the generation of very large velocity and pressure fluctuations that appear near the corner if the two perpendicular parts of the wall are joined directly (see Section 6.2).

4.2. Time Stepping

The density is evaluated by using the kernel estimate of the continuity equation (19), and the time step is performed with an Euler forward explicit algorithm. The pressure is evaluated by using the equation of state (9). To update velocities and positions, the Verlet algorithm was used,

$$\mathbf{r}_{n+1} = \mathbf{r}_n + \Delta t \mathbf{v}_n + \frac{1}{2}\Delta t^2 \left(\frac{d\mathbf{v}}{dt}\right)_n,$$
$$\mathbf{v}_{n+1/2} = \mathbf{v}_n + \frac{1}{2}\Delta t \left(\frac{d\mathbf{v}}{dt}\right)_n, \tag{27}$$

where Δt is the time step, $\mathbf{r}_n$ is the position vector of the SPH particle, $\mathbf{v}_n$ is the velocity, and $(d\mathbf{v}/dt)_n$ is the acceleration at the time step n. The acceleration term corresponding to the time step $n + 1$ is evaluated by using the position vector at the time step $n + 1$ and the velocity vector at the time step $n + \frac{1}{2}$, in Eqs. (22) and (23). Then the velocity at the time step $n + 1$ is evaluated as

$$\mathbf{v}_{n+1} = \mathbf{v}_{n+1/2} + \frac{1}{2}\Delta t \left(\frac{d\mathbf{v}}{dt}\right)_{n+1}. \tag{28}$$

This algorithm has second-order accuracy in Δt.

Notice that the stress-tensor components in Eqs. (22) and (23) depend on the strain-rate tensor through (24). As mentioned above, in order to evaluate the acceleration at the time step $n + 1$, the position vector at the time step $n + 1$ and the velocity vector at the time step $n + \frac{1}{2}$ are used. To evaluate the sums in Eqs. (22) and (23), one also needs the stress tensor and the strain-rate tensor at the time steps $n + 1$. In order to obtain the strain-rate tensor at the time step $n + 1$, a loop is performed in which the sums in Eq. (24) are evaluated using the position vector at the time step $n + 1$ and the velocity vector at the time step $n + \frac{1}{2}$. Once the strain-rate tensor at the time step $n + 1$ is known, the stress tensor is evaluated by using (7) and (8). Then a second loop is used to evaluate the acceleration terms in Eqs. (22) and (23). In this manner, when the acceleration terms at the time step $n + 1$ are evaluated, the position vector and the stress tensor both correspond to the time step $n + 1$ (the velocity is at time step $n + \frac{1}{2}$).

One possible approach to assure the stability of the scheme, is to set the time step so that it satisfies the Courant–Friedrichs–Lewy (CFL) condition. In order to set Δt, Libersky *et al.* [4] suggest the minimum over all particles of the expression

$$\Delta t = \frac{Ch}{(c + s)}, \tag{29}$$

where c is the adiabatic sound speed, s is the particle speed, h is the smoothing length, and C is a proportionality constant. Libersky *et al.* [4] suggest a value of $C = 0.3$. The sound speed is obtained differentiating (9)

$$c = \sqrt{dP/d\rho} = \sqrt{\gamma(\rho_{\max} - \rho_0)/(\rho_{\max} - \rho)}. \tag{30}$$

It has to be pointed out that for the cases studied in this work, there exists the possibility that the time step is controlled by the viscous forces and not determined by the CFL condition. In order to examine the stability condition for such a case, we rewrite the momentum equations (4) and (5), using the definitions of the viscosity given by (7) and (8). We consider a one-dimensional problem, which will be treated in more detail in Section 6.1. The ice is assumed to flow parallel to a straight coast in the y direction (see also Fig. 4 in Section 6.1), and to behave as an incompressible material, so that the momentum equations reduce to

$$h_{\text{ice}}\frac{\partial P}{\partial x} = \rho h_{\text{ice}} f v + C_a(U_a\cos\alpha - V_a\sin\alpha) + C_w v\sin\beta, \tag{31}$$

$$\rho h_{\text{ice}}\frac{\partial v}{\partial t} = h_{\text{ice}}\frac{\partial \eta \partial v}{\partial x^2} + C_a(U_a\sin\alpha + V_a\cos\alpha) - C_w v\cos\beta. \tag{32}$$

In Eqs. (31) and (32) we have assumed the x component of the velocity u and the gradients in the y direction as zero.

As mentioned in Section 2 (cf. Eqs. (7) and (8)), when $\eta < \eta_{\max}$, the ice flows in a plastic manner, while when $\eta = \eta_{\max}$ the ice flows as a viscous fluid. In other words, when the strain rate is sufficiently small such that the viscosity η reaches the maximum value $\eta_{\max}$, the flow is viscous. In certain cases the ''viscous-like'' states can be attained through fluctuations in strain rate, even when the maximum value of the viscosity is not usually reached during the simulation. This is the case in the straight *marginal ice* zone presented in Section 6.1. This is further discussed in the numerical results. Here, it is sufficient to say that in this case the ''effective'' viscosity in the viscous flow is

smaller than the value used for $\eta_{\max}$; however, $\eta_{\max}$ can still be used to get an estimate of the time step necessary to ensure the stability of the scheme.

In order to get some insight into the time step required when the time step is controlled by the viscous terms, we use the stability condition required to integrate (32) using an Euler forward scheme. Assuming that the viscosity in (32) is constant, the stability criterion in the corresponding *finite difference scheme* would be

$$\Delta t < \Delta x^2 \Big/ \left(2\eta/\rho(1 - \cos \lambda \, \Delta x) + \frac{C_w \cos \beta}{\rho h_{\text{ice}}} \Delta x^2 \right), \quad (33)$$

where Δx would be the grid spacing in the finite difference solution and λ would be the wave number of the initial space perturbation. For the values of $\eta_{\max}$ used in the present work (Section 2), the first term in the denominator is much larger than the second term and one can approximate the stability condition as

$$\Delta t < \frac{\Delta x^2}{\eta/\rho}, \quad (34)$$

which shows the dependence of the time step on the viscosity.

5. DISCRETE-PARTICLE METHODS FOR THE SIMULATION OF BROKEN-ICE FIELDS

The discrete-particle method is a different approach which can be used to make comparisons with the SPH simulations of the broken-ice fields. In this section, we briefly review the features of this method and its implementation for the simulation of broken-ice fields (for a detailed description, see Refs. [15–17]). Discrete-particle simulations are based on molecular-dynamic type of approaches. Here, one does not assume any rheological behavior of the ice field. In its implementation, the ice floes are modeled as random-sized, rough inelastic disks that float on the water surface. The floes are driven by the wind force and by the water currents. Energy dissipation occurs due to collisions and friction between floes, as well as due to the water drag on the bottom surface of the floe. The frictional force between floes is of Coulomb type and the dissipation during the normal contacts is described by a constant coefficient of restitution.

The equation of motion for each individual floe is given by

$$m \frac{d\mathbf{v}}{dt} = mf\mathbf{k} \times \mathbf{v} + A_f \boldsymbol{\tau}_a - A_f \boldsymbol{\tau}_w + \sum_{i=1}^{n} \mathbf{F}_i, \quad (35)$$

where $\mathbf{v}$ is the velocity of the floe, A_f is the floe area, m is its mass, $\Sigma^n \mathbf{F}_i$ are the contact forces acting on the floe due to the interaction with its neighbours, and $\boldsymbol{\tau}_a$ and $\boldsymbol{\tau}_w$ are the air and water drag forces per unit of floe area, respectively. As a result of the frictional forces, the floes experience rotations about their axes. The conservation equation for the angular momentum is

$$I\ddot{\theta} = \sum_{i=1}^{n} \boldsymbol{\Gamma}_\mathbf{i}, \quad (36)$$

where $I = \frac{1}{2}mr^2$ is the moment of intertia, $\ddot{\theta}$ is the angular acceleration, and $\Sigma^n \boldsymbol{\Gamma}_\mathbf{i}$ is the sum of the torques due to the tangential contact forces with the neighbor floes and due to the water drag force on the bottom surface of the floe.

The normal contact force between floes was simulated by using the latching spring model of Walton and Braun [22]. In this model, the normal force is given by

$$N = \begin{cases} K_1 \nu & \text{for loading,} \\ K_2(\nu - \nu_0) & \text{for loading,} \end{cases}$$

where ν is the overlap and ν_0 is the overlap when the normal force reaches zero during the unloading phase (Fig. 3). By using different constants for the compaction and recovery phases, this model can account for the inelasticity of the collisions. The area in the force-overlap diagram that is enclosed during a loading-unloading cycle corresponds to the energy dissipated in the collision. The coefficient of restitution, i.e., the ratio of final to initial relative normal velocity between floes in a collision, is given by $e = \sqrt{K_1/K_2}$.

In order to simulate the tangential friction forces between disks (or floes) in contact, we used the incrementally slipping friction model [22]. This is based on theoretical models developed by Mindlin and Deresiewicz [23, 24] to calculate the

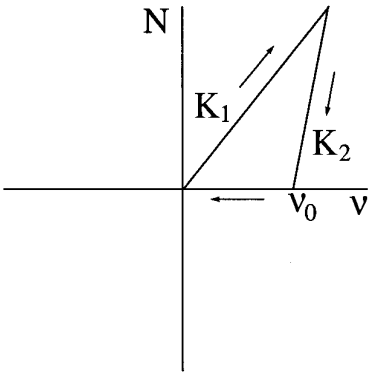

FIG. 3. Normal force vs overlap in the latching spring model of Walton and Braun [22].

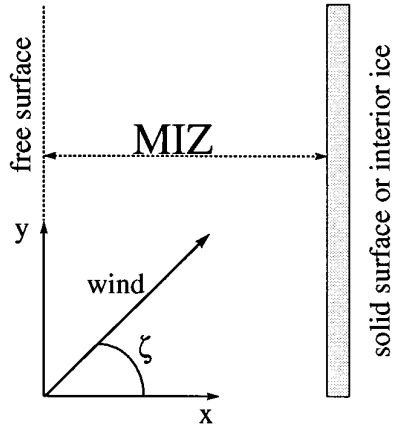

FIG. 4. Scheme of the simulation domain for the straight-coast problem. The origin of the x-coordinate is on the free surface; ζ is the angle between the geostrophic wind direction and the x axis.

friction forces between elastic spheres in contact. The model uses a nonlinear tangential spring, whose effective stiffness K_T, decreases with the relative displacement between the particles until it reaches zero when the ratio tangential to normal force satisfies the Coulomb friction condition ($F_t = \mu F_n$). This model is based on the assumption that the normal force is unaffected by small tangential displacements. This method is specially suitable for the simulation of quasi-static flows. A detailed description of its implementation can be found in Ref. [22]. Simpler approaches for more rapid flows can be found in Ref. [16].

In order to choose numerical values for the ice-floe parameters such as friction coefficient μ, coefficient of restitution e and spring constant K_1 used in the contact model we followed Ref. [16]. The values chosen for these parameters were: $K_1 = 2.5 \times 10^5$ N/m, $e = 0.7$, and $\mu = 0.3$.

6. SPH RESULTS AND COMPARISON WITH OTHER APPROACHES

6.1. Simulation of the Broken-Ice Field in the Presence of a Straight Coast

The simulation domain is shown in Fig. 4. It consists of a solid boundary on the right side of the domain and a free surface on the left side. The geostrophic wind velocity, V_a is constant and it makes an angle $\zeta = 45°$ with the horizontal axis (Fig. 4). Periodic boundary conditions are applied in the y direction. Hence, the problem can be considered as one-dimensional. Before the SPH results are presented, we show how an analytical approximation can be obtained for the one-dimensional problem.

6.1.1. *Analytical Approximation*

Assuming a steady, and fully developed flow in the y direction, the x and y components of the equations of motion (1) are given by [17]

$$C_a V_a(\cos\zeta\cos\alpha - \sin\zeta\sin\alpha) + (\rho h_{\text{ice}} f + C_w \sin\beta)v - h_{\text{ice}}\frac{dP}{dx} = 0, \tag{37}$$

$$C_a V_a(\cos\zeta\sin\alpha + \sin\zeta\cos\alpha) - C_w\cos\beta v - h_{\text{ice}}\frac{d\tau}{dx} = 0, \tag{38}$$

where $P = (\sigma_x + \sigma_y)/2$ and $\tau = \tau_{xy}$. The pressure at a distance x from the free surface is obtained by integrating (37)

$$P = \int_0^x \left[\frac{C_a V_a}{h_{\text{ice}}}(\cos\zeta\cos\alpha - \sin\zeta\sin\alpha) + \left(\rho f + \frac{C_w}{h_{\text{ice}}}\sin\beta\right)v\right]dx'. \tag{39}$$

In Eq. (39) the pressure has been assumed to be zero on the free surface ($x = 0$). Upon substitution of the shear stress from Eqs. (7) and (8) in Eq. (38), one can express the y component of the equation of motion as

$$C_a V_a(\cos\zeta\sin\alpha + \sin\zeta\cos\alpha) - C_w\cos\beta v + h_{\text{ice}}\sin\phi\frac{dP}{dx}\operatorname{sgn}\left[\frac{dv}{dx}\right] = 0, \tag{40}$$

where $\operatorname{sgn}[dv/dx]$ is the sign of dv/dx. Assuming that $\operatorname{sgn}[dv/dx] = -1$ (the maximum velocity is expected on $x = 0$, i.e., the free surface), dP/dx can be eliminated from Eqs. (37) and (40) and the following expression is obtained for the velocity:

$$v = \frac{C_a V_a[(\cos\zeta\sin\alpha + \sin\zeta\cos\alpha) + (\sin\zeta\sin\alpha - \cos\zeta\cos\alpha)\sin\phi]}{\rho h_{\text{ice}} f\sin\phi + C_w(\sin\beta\sin\phi + \cos\beta)} \tag{41}$$

The pressure is then obtained by substituting the velocity from Eq. (41) in Eq. (39).

In order to obtain (41), we have assumed that the stress state is on the yield envelope across the whole section. From (41) one obtains a constant velocity across the section. As shown below, a small velocity gradient is observed, however, the velocity profile does not deviate significantly from the constant velocity value obtained from (41). In Hibler's viscous-plastic approach [11] this small velocity gradient results from the presence of a viscous or creeping regime, which leads to stress states inside the yield envelope.

6.1.2. *Numerical Results*

In the SPH simulation, the magnitude of the wind velocity is $V_a = 9.3$ m/s. The value of the internal friction angle,

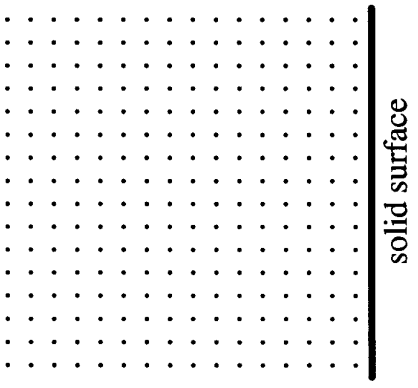

FIG. 5. Initial location of the SPH particles.

necessary to implement the Mohr–Coulomb rheology is given by $\sin \phi = 0.3$ (cf. (7) and (8)). The solid boundary conditions were implemented by using a wall that exerts a normal potential force of repulsion on the SPH particles, combined with a tangential frictional force (see Section 4). The value of the kernel parameter is $h = \Delta$, and this is kept constant in space and time. Initially, 256 SPH particles are located as shown in Fig. 5. The distance between particles corresponds to $\Delta = 7$ km. Initially, all the particles have zero velocity. Because of the wind drag and the Coriolis force, the particles are pushed against the wall until these forces are compensated by the pressure gradient. Once the steady state is reached, the particles move parallel to the solid surface. The steady state is attained approximately after a simulation equivalent to 16 h of real time. For the smallest time step used in these simulations, $\Delta t = 0.11$ s ($C = 0.005$ in Eq. (29)), this takes approximately 7.5 cpu hours on a Dec-Alpha (the total cpu time is inversely proportional to the value of the constant C). These times are considerable larger than those needed for solutions based on finite differences schemes. However, the main advantage of SPH is that it can be implemented very easily to handle the problem of moving boundaries (Section 6.2), while the implementation of Eulerian methods in fixed grids can become very complicated.

The constant velocity obtained from Eqs. (37) and (38) should be considered as a limiting value and a small velocity gradient is expected. Figure 6a shows velocity versus distance from the free surface, after 20 h of real time, for different values of the constant C (cf. 29). The velocity gradient indicates the presence of a viscous flow. However, this viscous flow does not result from the viscosity reaching the maximum value $\eta_{\max}$ in Eq. (8). Here, the viscous state is the result of small strain-rate fluctuations that lead to stress states inside the yield envelope and viscous flows.

One can see in Fig. 6a that when Δt decreases, the velocity profile converges and the velocity fluctuations are significantly reduced. Velocity fluctuations are analyzed by looking at the behavior of data points corresponding to the same x value (Figs. 4 and 5). Owing to the periodic boundary conditions, data corresponding to the same x value (same distance from the free surface) should collapse on the same data point in Fig. 6a. Dispersion in velocity values at constant distance from the free surface is a measure of the velocity fluctuations. One can see that for $\Delta t = 11$ s ($C = 0.05$), a large dispersion in velocity is observed, but this is significantly reduced for $\Delta t = 6.6$ s ($C = 0.03$). One can conclude from Fig. 6a that convergence to the final velocity profile occurs approximately for a time step between 1.1 s ($C = 0.05$) and 2.2 s ($C = 0.01$). Notice that for these values of the time step, the velocity fluctuations also have been considerable reduced. Libersky *et al.* have suggested to use a value of $C \sim 0.3$, which shows that in the present problem, the time step necessary to obtain a stable scheme is much smaller than the time step given by the CFL condition. The pressure (Fig. 6b) does not show any significant influence of the time step. The pressure has an important effect that arises from the on-

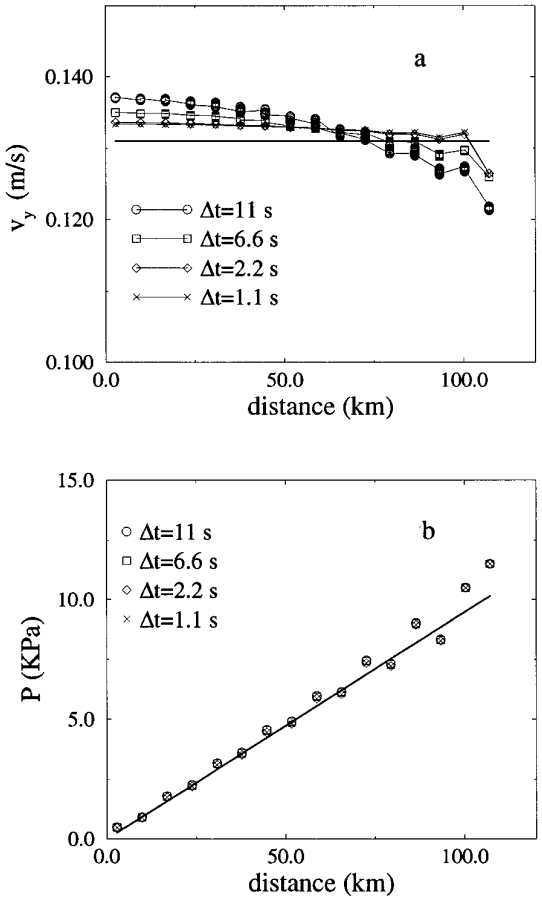

FIG. 6. (a) Velocity and (b) pressure vs distance from the free surface for different values of the time step. The solid lines are the analytical approximations according to Eqs. (39) and (41).

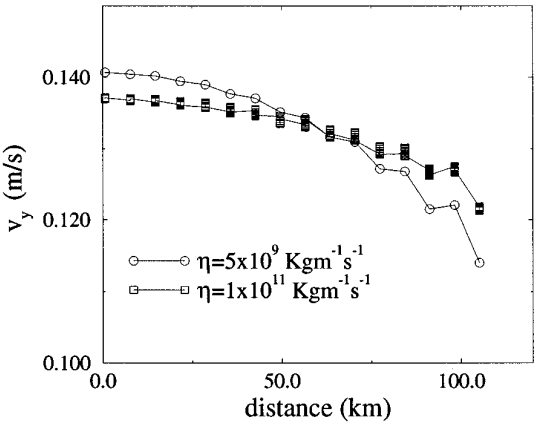

FIG. 7. Velocity vs distance from the free surface for two values of the viscosity $\eta_{\max}$ (cf. Eq. (8)), when the time step $\Delta t = 11$ s.

shore component of the wind velocity and its corresponding drag force on the ice, which is independent of the ice velocity.

If the viscous terms control the time step, Eq. (34) should give a better estimate of the time step requirements than the CFL condition. If one substitutes the maximum value of the viscosity (cf. Eq. (8)) used in the present simulations $\eta_{\max} = 1 \times 10^{11}$ Kg m^{-1} s^{-1} in (34), and assumes $\Delta x = 7$ Km (this is the initial distance between SPH particles), one obtains $\Delta t \sim 0.5$ s. This shows that the time steps which were necessary to obtain a stable algorithm are close to the value obtained when assuming that the time step is controlled by the viscous terms. In order to further test whether the viscous terms are indeed controlling the time step, we ran an additional simulation, using $\eta_{\max} = 5 \times 10^9$ Kg m^{-1} s^{-1} in Eq. (8). In this manner one forces the ice to behave as a viscous fluid with a viscosity 20 times smaller than the viscosity $\eta_{\max}$ of the previous simulations. Substituting $\eta_{\max} = 5 \times 10^9$ Kg m^{-1} s^{-1} in Eq. (8) one obtains $\Delta t = 10$ s. Hence, in this case if the viscous terms control the time step, one can use much larger time steps while still obtaining a stable scheme. Figure 7 shows the velocity profile obtained after 20 h or real time, for $\eta_{\max} = 5 \times 10^9$ Kg m^{-1} s^{-1} and $\eta_{\max} = 1 \times 10^{11}$ Kg m^{-1} s^{-1}, when $\Delta t = 11$ s. Significant velocity fluctuations are observed when $\eta_{\max} = 1 \times 10^{11}$ Kg m^{-1} s^{-1}, but a stable scheme is obtained when $\eta_{\max} = 5 \times 10^9$ Kg m^{-1} s^{-1}. This shows that in the present problem, the viscous terms control the time step and (8) gives a better estimate of the necessary time step than the CFL condition. It is important to point out that when one looks at a similar problem in a transient regime and without imposing periodic boundary conditions, much larger time steps can be used without giving rise to significant velocity fluctuations, even when $\eta_{\max} = 1 \times 10^{11}$ Kg m^{-1} s^{-1} (Section 6.2).

In order to test whether there exists any effect of the value of the constant β_{bc} (cf. (25)) on the velocity profiles, simulations were run for different values of β_{bc}. The value of the constant in Eq. (29) is $C = 0.03$ in all the cases. The value of the constant β_{bc} in Eq. (25), determines the distance between the wall and the SPH particles in the final-state configuration. Once the value of β_{bc} in Eq. (25) is large enough, the velocity profile obtained is independent of the value chosen for β_{bc}. This is shown in Fig. 8, where the velocity versus distance from the free surface, after 16 h of real time, is plotted for three different values of β_{bc}. Once β_{bc} is large enough, further increases in the value of β_{bc} have almost no effect on the distance between the SPH particles and the wall in the final configuration. Thus, once this asymptotic regime is reached, the value chosen for β_{bc} has a negligible influence on the final velocity profile.

6.2. Simulation of the Broken-Ice Field next to a Corner-Shaped Coast

The simulation domain consists of a free surface on the left-hand side and a corner-shaped coast on the right-hand side (Fig. 9). The geostrophic wind direction makes an angle $\zeta = 45°$ with the x axis. As in the case of the straight coast, the magnitude of the wind velocity was $V_a = 9.3$ m/s. The value of the internal friction angle was given by $\sin \phi = 0.3$ (cf. (7) and (8)). Initially, 834 SPH particles were located as shown in Fig. 10a. The initial distance between SPH particles corresponds to $\Delta = 7.1$ km. Notice that the two corners on the solid wall in Fig. 10a have been smoothed. Rounding the corners allows for a smooth transition between the perpendicular parts of the wall and avoids large velocity and pressure fluctuations that would appear otherwise in the nearby zones of the corners.

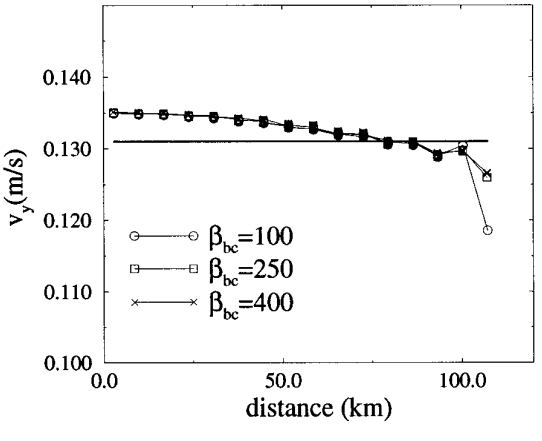

FIG. 8. Velocity vs distance from the free surface for different values of the constant β_{bc} in Eq. (25). The values of the constant β_{bc} have been nondimensionalized dividing them by $(\rho_{\text{ice}}\Delta^3 f^2)$. The solid line is the analytical approximation according to Eq. (41).

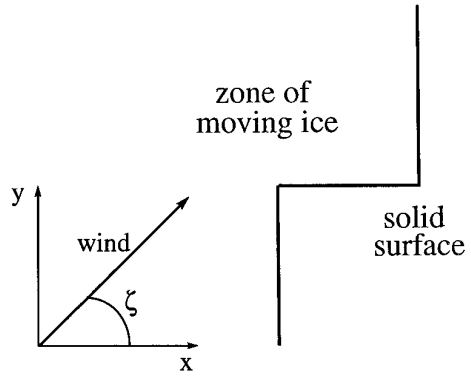

FIG. 9. Simulation domain for the corner-shaped coast. The origin of the coordinate system is on the left-lower corner of the initial ice-field domain (see Fig. 10); ζ is the angle between the geostrophic wind direction and the x axis.

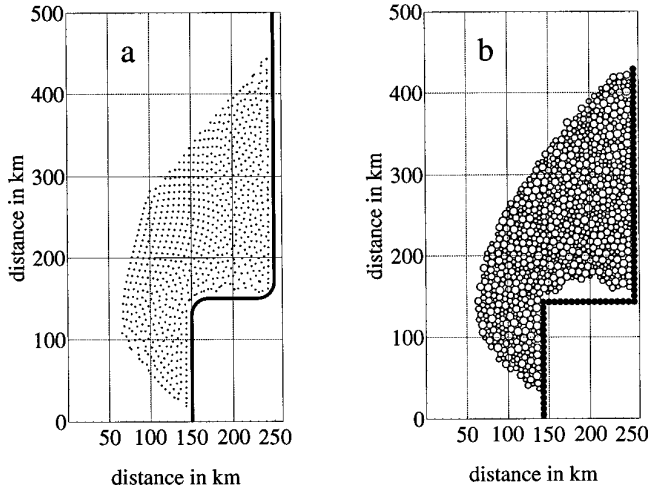

FIG. 11. (a) SPH-particle locations and (b) ice-floe positions after a simulation corresponding to a real time of approximately 9.5 days. The deformation of the ice field obtained in the SPH simulation is in reasonable agreement with that obtained in the discrete-particle simulation.

In this section, we compare the results of the SPH simulations with the results obtained by using discrete-particle simulations. Initially, 824 floes were distributed as shown in Fig. 10b. In order to avoid order effects that can arise from using equal-sized disks, the floes are modeled as random-sized disks. Their diameters are uniformly distributed between 4 km and 10 km.

The location of SPH particles and the ice floes in the discrete-particle simulations after a time equalivalent to 9.5 days is shown in Fig. 11a and Fig. 11b, respectively (the SPH simulation takes approximately 7 cpu hours on a Dec-Alpha). One can see by comparing Fig. 11a and Fig. 11b that the deformation of the ice field predicted by the two methods are in reasonable agreement. One of the main advantages of SPH is its ability to clearly predict the location of the edge. Using finite differences in an Eulerian fixed grid presents several problems that can be avoided in SPH: The edge location must be determined by means of a constant density contour and because of problems of artificial diffusion at the edge, it is not possible to obtain a sharp definition of the edge location. Defining boundary conditions such as normal derivatives on the free surface (which sometimes can be a very complicated shape) must be done by using a very fine grid. In order to correctly handle the problem of the moving boundary in the framework of an Eulerian fixed grid, complicated semi-Lagrangian approaches have to be adopted.

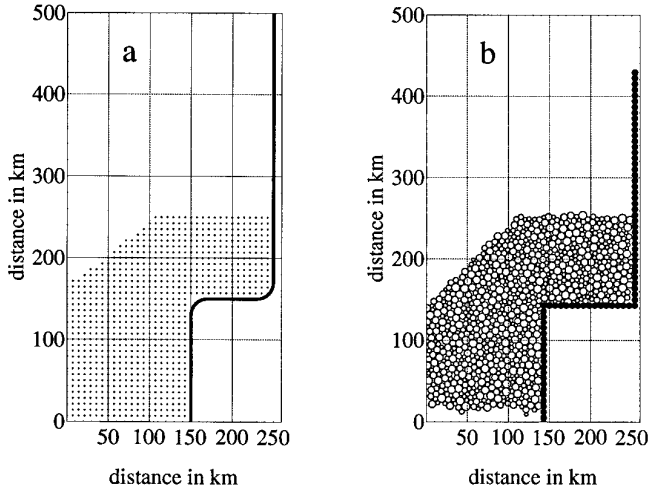

FIG. 10. Initial distribution of particles for (a) the SPH simulation and (b) the discrete-particle simulation. In (a) the thick line is the solid surface and in (b) the black particles are fixed particles which model the solid surface.

Figure 12 shows the time series of the x components (Fig. 12a) and the y component (Fig. 12b) of the velocity at a location centered at $(x, y) = (140, 220)$ km. Velocities corresponding to two values of the constant C in Eq. (29) are shown in Fig. 12 ($C = 0.1$ and $C = 0.05$). Notice that the values used for C (and the corresponding time steps) are an order of magnitude larger than those used in the case of the straight coast (Section 6.1). For this simulation, a value of $C = 0.1$ can be considered as reasonable. Decreasing further the value of C (and the time step) has a negligible effect on the velocity. Further increases in the value of C starts to generate some high frequency fluctuations in the x component of the velocity. However, these fluctuations are not significant and there can be some increase in the time step. Similar conclusions can be drawn from the time series of the velocity and pressure at different locations (these results will be presented in detail elsewhere). Unlike the case of the straight coast, it is the CFL

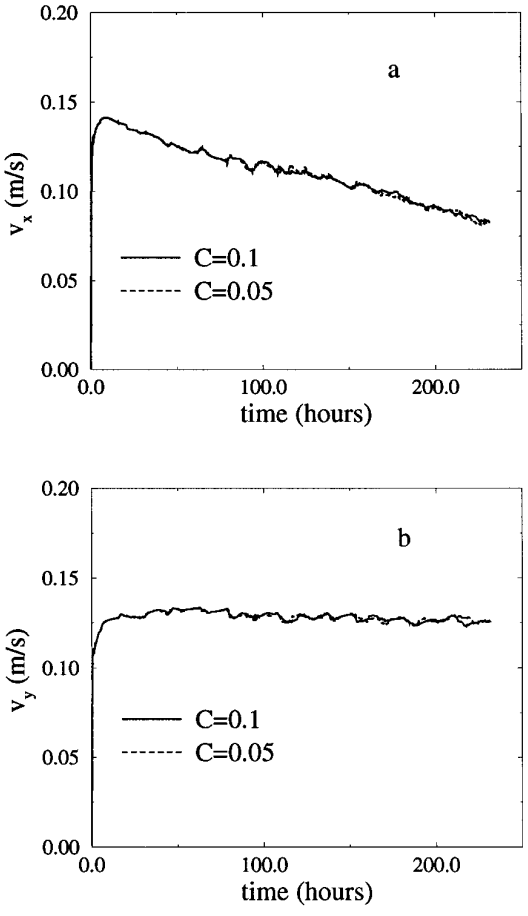

FIG. 12. Velocity vs time at a coordinate $(x, y) = (140, 220)$ km. The time series obtained for both values of the constant C are in reasonable agreement. Hence, $C = 0.1$ in Eq. (29) can be considered as appropriate to set the value of the time step for this problem.

condition that controls the time step in the present problem.

7. CONCLUSIONS

We have implemented a Mohr–Coulomb type rheology in the framework of SPH. In systems described by this type of rheological behavior, one also needs to model frictional walls through boundaries in which the Coulomb-friction condition is satisfied. We have proposed a method for modelling the frictional boundary conditions, which we have shown is able to predict correctly the effect of this type of boundary. From the present results, one concludes that SPH is a powerful tool for the simulation of systems characterized by a rheology of Mohr–Coulomb type. It has important advantages in comparison with standard finite differences approaches, when it is applied to problems that involve both frictional solid surfaces and free surfaces. As was previously mentioned, this type of rheological behavior can be found not only in ice-broken fields, but in numerous problems in the field of quasi-static granular flows.

The Mohr–Coulomb yield criterion in the framework of the viscous-plastic approach gives rise to a rheology in which the stress is a nonlinear function of the strain-rate. According to the present results, SPH has been successfully applied for the simulation of this type of nonlinear rheology. It is possible that SPH can be applied to solve other problems involving fluids in which the stress-strain rate relations are described by nonlinear rheologies.

ACKNOWLEDGMENTS

The authors are grateful to the Natural Sciences and Engineering Research Council of Canada (NSERC) for financial support through an NSERC Strategic Grant titled ''Mesoscale ice rheology for regional ice forecasting.'' We also thank Mohamed Sayed for very useful suggestions during this work.

REFERENCES

1. L. B. Lucy, A numerical approach to the testing of the fission hypothesis, *Astronom. J.* **82,** 1013 (1977).
2. R. A. Gingold and J. J. Monaghan, Smoothed particle hydrodynamics: Theory and application to non-spherical stars, *Mon. Notes R. Astronom. Soc.* **181,** 375 (1977).
3. L. D. Libersky and A. Petschek, Smooth particle hydrodynamics with strength of materials, in *The Next Free Lagrange Conference*, edited by H. Trease, J. W. Fritts, and W. P. Crowley (Springer-Verlag, Jackson Hole, WY, 1992), 248.
4. L. D. Libersky *et al.*, High strain Lagrangian hydrodynamics, *J. Comput. Phys.* **109,** 67 (1993).
5. A. G. Petschek and L. D. Libersky, Cylindrical smoothed particles hydrodynamics, *J. Comput. Phys.* **109,** 76 (1993).
6. W. Benz and E. Asphaug, Impact simulations with fracture. I. Method and tests, *Icarus* **107,** 98 (1994).
7. H. Takeda, S. M. Miyama, and M. Sekeiya, Numerical simulation of viscous flow by smoothed particle hydrodynamics, *Progr. Theor. Phys.* **92,** 939 (1994).
8. D. Rothrock, The energetic of plastic deformation of pack ice by ridging, *J. Geophys. Res.* **3,** 4514 (1975).
9. R. Pritchard, An elastic-plastic constitutive model for sea ice, *J. Appl. Mech.* **43E,** 379 (1975).
10. W. Hibler, A viscous sea ice law as a stochastic average of plasticity, *J. Geophys. Res.* **82,** 3932 (1977).
11. W. Hibler, A dynamic thermodynamic sea ice model, *J. Phys. Oceanogr.* **9,** 815 (1979).
12. R. Pritchard, A. Mueller, D. Hanzlick, and Y. Yang, Forecasting Bering sea ice edge behavior, *J. Geophys. Res.* **95,** 775 (1990).
13. M. G. Flato, A particle in cell sea-ice model, *Atmosphere-Ocean* **31,** 339 (1993).
14. J. J. Monaghan, Simulating free surface flows with SPH, *J. Comput. Phys.* **110,** 399 (1994).
15. S. B. Savage, Marginal ice zone dynamics modelled by computer simulations involving floe collisions, *Report for Contract 91-1547/5471* (IME of National Research Council, Canada, 1992).
16. S. B. Savage, Marginal ice zone dynamics modeled by computer

simulations involving floe collisions, in *Mobile Particulate Systems*, edited by E. Guazelli and L. Oger (Kluwer Academic, Netherlands, 1995), 305.

17. R. Gutfraind and S. B. Savage, Marginal ice zone rheology: Comparison of results from continuum plastic models and discrete particle simulations, preprint, 1996.
18. M. G. McPhee and J. D. Smith, An analysis of pack ice drift in summer, in *Sea Ice Processes and Models*, edited by R. Pritchard (Univ. of Washington Press, Seattle, 1980), p. 62.
19. J. J. Monaghan, An introduction to SPH, *Comput. Phys. Commun.* **48,** 89 (1988).
20. J. J. Monaghan, Smoothed particle hydrodynamics, *Annu. Rev. Astronom. Astrophys.* **30,** 543 (1992).
21. W. Benz, Smoothed particle hydrodynamics: A review, in *The Numerical Modeling of Nonlinear Stellar Pulsations*, edited by J. Buchler (Kluwer, Dordrecht, 1990).
22. O. Walton and R. Braun, Viscosity and temperature calculations for assemblies of inelastic frictional disks, *J. Rheology* **30,** 949 (1986).
23. R. Mindlin, Compliance of elastic bodies in contact, *J. Appl. Mech.* **16,** 259 (1949).
24. R. Mindlin and H. Deresiewicz, Elastic spheres in contact under varying oblique forces, *J. Appl. Mech.* **20,** 327 (1953).